

Distributed Affine Body Dynamics with Adaptive Consensus

JIAFENG LIU, State Key Lab of CAD and CG, Zhejiang University, China
 WENHUI ZHOU, State Key Lab of CAD and CG, Zhejiang University, China
 XINMING PEI, State Key Lab of CAD and CG, Zhejiang University, China
 YIFAN PENG, The University of Hong Kong, China
 HUAMIN WANG, Style3D Research, China
 YIN YANG, University of Utah, USA
 LEI LAN*, State Key Lab of CAD and CG, Zhejiang University, China
 WEIWEI XU, State Key Lab of CAD and CG, Zhejiang University, China

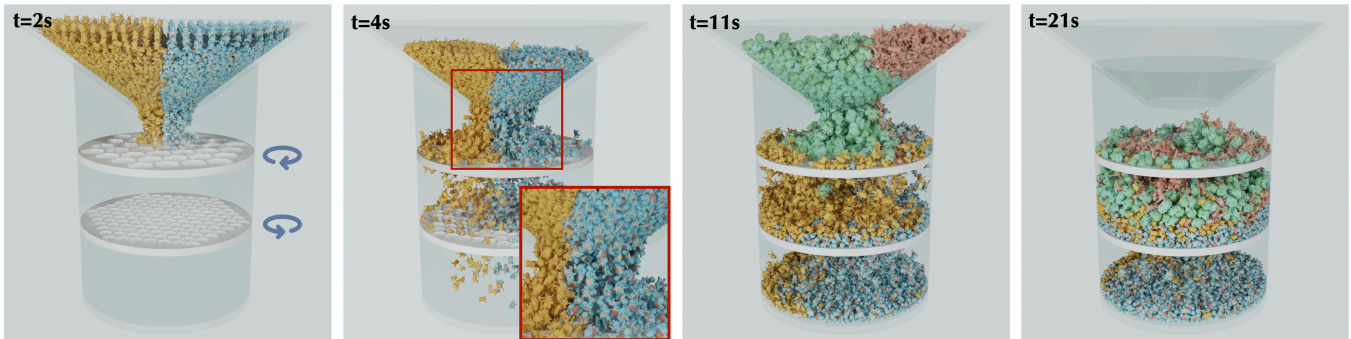


Fig. 1. A contact-rich simulation in which 5K “Pokémon” ABD bodies (6M triangles in total) fall into a narrow funnel under a two-worker distributed simulation setup. After entering the lower chamber, the bodies interact with two perforated turntables rotating in opposite directions, producing sustained stacking and recurring collisions. Our system remains penetration-free throughout the simulation despite complex geometry and cross-worker contacts.

Affine Body Dynamics (ABD) within the Incremental Potential Contact (IPC) framework provides accurate simulation of extremely stiff solids exhibiting near-rigid behavior, with strict non-penetration guarantees. However, IPC’s globally coupled barrier constraints hinder scalable execution across multiple GPUs and compute nodes. We propose a distributed formulation of ABD using a consensus-based ADMM scheme. Each compute node solves its local ABD subproblem in parallel, followed by a global consensus step that enforces consistency among shared boundary bodies. The proposed method preserves IPC-level robustness and global consistency under distributed execution. Experiments demonstrate stable convergence, non-penetration, and efficient scaling on large-scale scenes across multiple nodes.

*Corresponding author.

Authors’ Contact Information: Jiafeng Liu, State Key Lab of CAD and CG, Zhejiang University, Hangzhou, China, jiafengliu@zju.edu.cn; Wenhui Zhou, State Key Lab of CAD and CG, Zhejiang University, Hangzhou, China, wenhuizhou@zju.edu.cn; Xinming Pei, State Key Lab of CAD and CG, Zhejiang University, Hangzhou, China, xmpei@zju.edu.cn; Yifan Peng, The University of Hong Kong, Hong Kong, China, evanpeng@hku.hk; Huamin Wang, Style3D Research, Hangzhou, China, wanghmin@gmail.com; Yin Yang, University of Utah, Salt Lake City, USA, yangzzy@gmail.com; Lei Lan, State Key Lab of CAD and CG, Zhejiang University, Hangzhou, China, leilan@zju.edu.cn; Weiwei Xu, State Key Lab of CAD and CG, Zhejiang University, Hangzhou, China, xww@cad.zju.edu.cn.



This work is licensed under a Creative Commons Attribution 4.0 International License. *SIGGRAPH Conference Papers ’26, Los Angeles, CA, USA*
 © 2026 Copyright held by the owner/author(s).
 ACM ISBN 979-8-4007-2554-8/2026/07
<https://doi.org/10.1145/3799902.3811106>

CCS Concepts: • **Computing methodologies** → **Distributed simulation**.

Additional Key Words and Phrases: Distributed simulation; Affine body dynamics; Incremental potential contact; ADMM

ACM Reference Format:

Jiafeng Liu, Wenhui Zhou, Xinming Pei, Yifan Peng, Huamin Wang, Yin Yang, Lei Lan, and Weiwei Xu. 2026. Distributed Affine Body Dynamics with Adaptive Consensus. In *Special Interest Group on Computer Graphics and Interactive Techniques Conference Papers (SIGGRAPH Conference Papers ’26)*, July 19–23, 2026, Los Angeles, CA, USA. ACM, New York, NY, USA, 11 pages. <https://doi.org/10.1145/3799902.3811106>

1 Introduction

Simulating materials that behave nearly rigid under contact is a recurring challenge in contact-rich physical interaction, particularly in embodied intelligence [Barreiros et al. 2025; Long et al. 2025]. In such settings, even minor violations of non-penetration can qualitatively alter interaction outcomes. The Incremental Potential Contact (IPC) framework [Li et al. 2020a] demonstrates that barrier-based formulations can robustly enforce non-penetration constraints under dense and dynamic contact. Within this framework, Affine Body Dynamics (ABD) [Lan et al. 2022a] provides a practical model for near-rigid materials by representing each body with 12 affine degrees of freedom, balancing numerical robustness and computational efficiency. Compared to conventional rigid body motion, ABD produces linear vertex trajectories over time, which simplifies continuous collision detection (CCD) in contact-rich scenarios.

Scaling ABD to large-scale scenes with dense contact remains challenging. As scene complexity grows, the number of degrees of freedom increases rapidly, making single-device solvers inefficient due to the cost of assembling and solving large coupled systems. Dense contact configurations can generate tens to hundreds of millions of candidate collision pairs, incurring substantial overhead in collision detection and contact processing. While scaling ABD across parallel or distributed hardware is a natural way to overcome these limitations, in practice, barrier-based contact formulations introduce strong global coupling across interacting objects, causing naive domain decomposition and local solve strategies to fail.

In light of these challenges, we propose a distributed simulation framework for ABD that runs across multiple compute nodes in parallel and maintains penetration-free contact throughout the simulation. In contact-rich scenarios, IPC contact constraints introduce strong coupling among interacting bodies. As a result, distributed ABD simulation constitutes a *consensus optimization* problem in which consistency must be enforced on the states of bodies shared across partitions to ensure a well-defined global solution.

We solve this optimization problem using the Alternating Direction Method of Multipliers (ADMM), which decomposes a global optimization problem into local subproblems and enforces consistency among them through augmented Lagrangian updates. The convergence of ADMM is known to be sensitive to the choice of the penalty parameter ρ , particularly in strongly coupled distributed problems. To address this challenge, we introduce an adaptive consensus mechanism that regulates the strength of consistency enforcement by adaptively adjusting the penalty parameter ρ . We adopt a mass-aware strategy to initialize ρ based on body masses, and further refine it through residual-driven adaptation during the iterations. Mass-aware initialization establishes a stable baseline, while adaptive consensus dynamically maintains balanced progress among heterogeneous subproblems, resulting in faster and more stable convergence across partitions.

In addition, ensuring non-penetration in contact-rich distributed simulation requires particular care. Even if local updates remain penetration-free under the IPC barrier energy, naive synchronization across partitions can still introduce interpenetration. To address this, we introduce a *feasibility-preserving consensus* mechanism that combines locally valid updates with a global, CCD-certified consensus step, applying synchronized states only when they pass the CCD check. This supports stable, penetration-free simulation at large scale, handling thousands of rigid bodies with surface meshes containing tens of millions of triangles, while maintaining strong parallel scalability in distributed environments.

In summary, this work makes the following contributions:

- We present a distributed ABD framework based on ADMM that preserves IPC-style non-penetration guarantees while enabling scalable execution across multiple GPUs and compute nodes for large-scale, contact-rich simulations.
- We propose a mass-aware initialization of the ADMM penalty parameter, combined with residual-driven adaptation, which accelerates convergence and improves robustness in distributed ABD optimization.
- We demonstrate the effectiveness of the proposed method on large-scale, contact-rich simulation scenarios, showing stable

convergence, penetration-free simulation, and efficient scaling in distributed environments.

2 Related Work

ADMM for simulation. ADMM is widely used in physics-based simulation. By decomposing a global optimization into simple, parallelizable subproblems, it enables efficient solvers for fluids [Inglis et al. 2017; Pan and Manocha 2017], elastic bodies [Brown and Narain 2021; Daviet 2023; Fang et al. 2019; Overby et al. 2017], multibody systems [Ji et al. 2025; Lee et al. 2023], and contact handling [Chen et al. 2023; Daviet 2020; Tasora et al. 2021]. However, ADMM often slows down near convergence. Recent work accelerates ADMM by viewing it as a fixed-point iteration and applying Anderson acceleration or Douglas-Rachford splitting (DRS)-based reformulations [Ouyang et al. 2020; Peng et al. 2018; Zhang et al. 2019]. ADMM is also sensitive to the penalty parameter. For deformable simulation, prior methods tune it using stiffness/curvature proxies to balance local and global updates [Brown and Narain 2021; Daviet 2020; Fang et al. 2019; Overby et al. 2017]. This strategy is less effective in our distributed ABD setting. We instead adopt a mass-aware penalty with residual-driven updates, which substantially improves convergence in our system.

Penetration-free contact handling. Penetration-free contact is essential for physics-based simulation, as interpenetration undermines plausibility and can destabilize contact response. Incremental Potential Contact (IPC) [Li et al. 2020a] is a robust interior-point framework that maintains a feasible optimization path using CCD-based line search and a barrier contact energy. IPC has been extended to cloth [Lan et al. 2024; Li et al. 2020b, 2023], rigid (or close-to-rigid) bodies [Chen et al. 2022; Ferguson et al. 2021; Lan et al. 2022a], and fluid-rigid coupling [Xie et al. 2023], but its computational cost has motivated many acceleration efforts. Recent GPU-oriented advances include coordinate descent [Lan et al. 2023], Gauss-Newton Hessian approximations [Huang et al. 2024a], MAS-preconditioned ABD-IPC [Huang et al. 2024b], and barrier-augmented Lagrangian variants [Guo et al. 2024]. Besides, non-barrier alternatives also provide efficient solutions [Chen et al. 2025; Lan et al. 2024; Wang et al. 2023; Zheng et al. 2025]. Local-global methods [Lan et al. 2022b; Li et al. 2023] are particularly relevant due to their alternating structure. PD-IPC [Lan et al. 2022b] replaces nonlinear barrier iterations with massively parallel local projections and a global linear solve. Our method adopts a similar local/merge alternation, but treats the ADMM consensus state as an intermediate estimate and enforces penetration-freeness only at termination.

Distributed optimization. Prior research on distributed optimization spans both optimization methods, such as decomposition [Chan and Mathew 1994; Palomar and Chiang 2006] and consensus-based optimization schemes [Boyd et al. 2011; Nedic and Ozdaglar 2009; Shi et al. 2015; Yang et al. 2022; Yuan et al. 2018], and system frameworks for large-scale distributed execution [Dean and Ghemawat 2008; Fetterly et al. 2009; Gropp 2001; Low et al. 2012; Zaharia et al. 2012]. These ideas naturally connect to distributed simulation, where physical systems are partitioned across devices and coordinated through cross-partition communication. P-cloth [Li et al. 2020c]

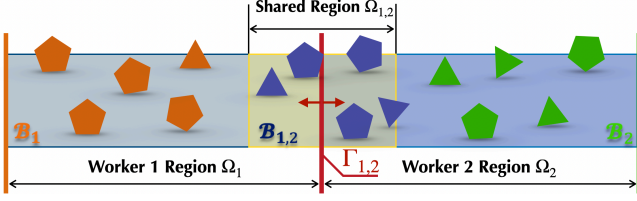


Fig. 2. Partition model. The entire scene is partitioned into two regions (Ω_1, Ω_2) by the boundary $\Gamma_{1,2}$. We set up an overlap area as *Shared Region* $\Omega_{1,2}$ around $\Gamma_{1,2}$. Objects with the same color belong to the same set. Orange and green denote the sets of internal bodies of worker 1 (\mathcal{B}_1) and worker 2 (\mathcal{B}_2), respectively, while blue indicates the geometry of the *shared bodies*. Note that the partition boundary $\Gamma_{1,2}$ is a plane that can only translate along its normal direction, as indicated by the red arrows in the figure.

distributes the dominant linear solve for implicit cloth stepping across multiple GPUs. Rustico et al. [2012] propose a distributed SPH fluid solver with dynamic load balancing, and Liu et al. [2016] develop a scalable Eulerian method via a Schur-complement formulation. *Nimbus* further automates distributed execution for grid-based fluids [Mashayekhi et al. 2018]. Wang et al. [2020] exchange the halo-region data of MPM between GPU partitions. Qiu et al. [2023] extend this line with sparse grids on GPU-equipped supercomputers. Brown et al. [2020] use aura-based migration to co-locate potentially colliding rigid bodies, and *Loki* [Lesser et al. 2022] targets multi-physics parallel execution across multiple CPU compute nodes.

Prior work has explored split-and-merge style strategies for parallel and distributed simulation. Kale and Kry [2023] use overlapping interface-body sets with state blending. Tonge et al. [2012] introduce mass splitting, and Daviet [2023] applies a similar split-and-average idea to GPU-parallel contact projection across multiple GPUs. These works are closely related to our method in that they all rely on duplicating interface states and reconciling them through a merge step. However, they do not address high-accuracy collision response with strict non-penetration enforcement in contact-rich distributed simulation.

3 Preliminaries

Implicit Euler integration via optimization. The backbone formulation of our framework follows ABD, which advances the simulation by solving the following variational problem:

$$\mathbf{q}^{t+1} = \arg \min_{\mathbf{q}} \frac{1}{2} \|\mathbf{q} - \tilde{\mathbf{q}}\|_{\mathbf{M}}^2 + h^2 E_{ARAP}(\mathbf{q}) + h^2 E_{IPC}(\mathbf{q}), \quad (1)$$

where \mathbf{q} denotes the generalized coordinates of the system, \mathbf{M} is the mass matrix of affine bodies, E_{ARAP} and E_{IPC} are the elastic energy and collision energies, respectively. $\tilde{\mathbf{q}} = \mathbf{q}^t + h\dot{\mathbf{q}} + h^2 \mathbf{M}^{-1} \mathbf{f}_{ext}^{t+1}$ is the predicted position based on the inertia and external forces, where h is the time step and \mathbf{f}_{ext} is the external generalized force. For detailed definitions of the DoFs and energy terms, we refer to the prior work [Lan et al. 2022a].

4 Distributed Simulation with Consensus

For clarity, we first introduce the distributed formulation. Fig. 2 provides a concrete example of two workers. We consider a distributed system with N workers, indexed by $\mathcal{W} := \{1, \dots, N\}$. Let

$\mathcal{B} := \{b_1, b_2, \dots, b_B\}$ denote the set of bodies in the scene, where $B = |\mathcal{B}|$. Each worker communicates only with its neighboring workers. For worker i , let \mathcal{N}_i denote its neighbor set. By definition, $i \notin \mathcal{N}_i$, and the neighbor relation is symmetric: $j \in \mathcal{N}_i \Leftrightarrow i \in \mathcal{N}_j$. We partition the scene into sub-regions $\{\Omega_i\}$ and assign worker i to region Ω_i . For neighboring workers i and j (with $j \in \mathcal{N}_i$), we denote their interface by Γ_{ij} and introduce a shared overlap region Ω_{ij} to capture cross-interface interaction. Under this model, worker i maintains two collections of bodies: \mathcal{B}_i , the internal bodies of worker i , and \mathcal{B}_{ij} , the bodies shared with neighbor j . These shared bodies constitute the interface variables whose states are duplicated across workers and coordinated through consensus in the distributed formulation. For the overlap-region width, we use $w = \max(\alpha v_{\max} dt, w_{\min})$ with $\alpha = 2$, where v_{\max} is the maximum body velocity and w_{\min} is the smallest body-bounding-box diagonal. The first term prevents missed bodies across one time step, and the second prevents an overly narrow shared region at low velocity.

4.1 Consensus ADMM Solver

Problem definition. We now define the optimization problem solved at each time step using ADMM. The global ABD system is partitioned across N workers and solved in a distributed manner, which naturally gives rise to a *consensus optimization* problem:

$$\min_{\{\mathbf{q}_i\}, \{\mathbf{z}_b\}} \sum_{i=1}^N F_i(\mathbf{q}_i), \quad \text{s.t. } \mathbf{q}_{i,b} - \mathbf{z}_b = 0, \quad \forall i = 1, \dots, N, \quad \forall b \in \mathcal{B}_{i,\partial}. \quad (2)$$

where $\mathcal{B}_{i,\partial} := \bigcup_{j \in \mathcal{N}_i} \mathcal{B}_{ij}$ denotes the set of shared bodies handled by worker i , and $\{\mathbf{z}_b\}_{b \in \mathcal{B}_{i,\partial}}$ are the consensus variables, with $\mathcal{B}_{i,\partial} := \bigcup_{i=1}^N \mathcal{B}_{i,\partial}$. The vector \mathbf{q}_i stacks the local DoFs maintained by worker i , including replicas of shared bodies, and $\mathbf{q}_{i,b}$ denotes the DoFs block corresponding to body b within \mathbf{q}_i . A naive summation $\sum_i F_i$ would over-count contributions associated with replicated bodies or cross-partition interactions, which motivates the consensus formulation.

To ensure consistency of the global objective with the single-worker formulation, we normalize these contributions by their replication counts. Specifically, let κ_b denote the number of workers that hold a replica of body b , and let κ_c denote the number of workers that include a contact pair c .

The local objective on worker i is defined as

$$F_i(\mathbf{q}_i) = \sum_{b \in \mathcal{B}_i \cup \mathcal{B}_{i,\partial}} \frac{1}{\kappa_b} \left(\frac{1}{2} \|\mathbf{q}_{i,b} - \tilde{\mathbf{q}}_{i,b}\|_{\mathbf{M}_{i,b}}^2 + h^2 E_{ARAP}(\mathbf{q}_{i,b}) \right) + h^2 \sum_{c \in \mathcal{C}_i} \frac{1}{\kappa_c} \phi_c(\mathbf{q}_i), \quad (3)$$

where \mathcal{C}_i is the set of IPC contact pairs on worker i , and $\phi_c(\cdot)$ is the IPC barrier term for pair c . This construction ensures that each per-body and contact-pair term contributes exactly once to the global objective $\sum_i F_i$.

We apply ADMM to Eq. (2) by constructing the augmented Lagrangian in scaled form [Boyd et al. 2011]:

$$\mathcal{L} = \sum_{i=1}^N \left(F_i(\mathbf{q}_i) + \sum_{b \in \mathcal{B}_{i,\partial}} \left[\frac{\rho_{i,b}}{2} \|\mathbf{q}_{i,b} - \mathbf{z}_b + \mathbf{u}_{i,b}\|^2 - \frac{\rho_{i,b}}{2} \|\mathbf{u}_{i,b}\|^2 \right] \right). \quad (4)$$

where \mathcal{L} denotes the scaled-form augmented Lagrangian, and we suppress its arguments for brevity, $\mathbf{u}_{i,b}$ denotes the scaled dual variable and $\rho_{i,b}$ is the penalty parameter. Starting from initial values $\{\mathbf{q}_i^0\}$, $\{\mathbf{z}_b^0\}$, and $\{\mathbf{u}_{i,b}^0\}$, ADMM alternates between local solves, consensus updates, and dual updates.

At iteration k , each worker i performs a local solve by minimizing F_i with respect to \mathbf{q}_i , while softly anchoring each shared body block $\mathbf{q}_{i,b}$ to the current consensus \mathbf{z}_b^k via a quadratic penalty weighted by $\rho_{i,b}$:

$$\mathbf{q}_i^{k+1} = \arg \min_{\mathbf{q}_i} F_i(\mathbf{q}_i) + \sum_{b \in \mathcal{B}_{i,\partial}} \frac{\rho_{i,b}}{2} \left\| \mathbf{q}_{i,b} - \mathbf{z}_b^k + \mathbf{u}_{i,b}^k \right\|^2. \quad (5)$$

A consensus step is then performed for each shared body b by aggregating the updated local blocks $\{\mathbf{q}_{i,b}^{k+1} + \mathbf{u}_{i,b}^k\}$ for $i \in \mathcal{W}_b$ across workers to obtain the new consensus variable \mathbf{z}_b^{k+1} :

$$\mathbf{z}_b^{k+1} = \arg \min_{\mathbf{z}_b} \sum_{i \in \mathcal{W}_b} \frac{\rho_{i,b}}{2} \left\| \mathbf{z}_b - \left(\mathbf{q}_{i,b}^{k+1} + \mathbf{u}_{i,b}^k \right) \right\|^2. \quad (6)$$

Here, $\mathcal{W}_b := \{i \in \mathcal{W} \mid b \in \mathcal{B}_{i,\partial}\}$ denotes the set of workers that store a local copy of body b . The dual update then adjusts the scaled multipliers $\mathbf{u}_{i,b}$ based on the current primal residual, gradually reducing discrepancies among replicated variables:

$$\mathbf{u}_{i,b}^{k+1} = \mathbf{u}_{i,b}^k + \mathbf{q}_{i,b}^{k+1} - \mathbf{z}_b^{k+1}. \quad (7)$$

Note that the \mathbf{z} update does not require a centralized worker. For each shared body b , every worker in \mathcal{W}_b can compute the same \mathbf{z}_b^{k+1} locally by exchanging $\{\mathbf{q}_{j,b}^{k+1}, \mathbf{u}_{j,b}^k, \rho_{j,b}\}$ with neighboring workers that hold replicas of b .

Stopping criteria. ADMM iterations are terminated based on three metrics: the Newton update magnitude $\|\Delta \mathbf{q}_i^{k+1}\|_\infty$, the primal residual r_∞^{k+1} , and the dual residual s_∞^{k+1} , all normalized by the scene scale l and evaluated using the ℓ_∞ norm:

$$\max_{i=1,\dots,N} \frac{1}{hl} \|\Delta \mathbf{q}_i^{k+1}\|_\infty < \theta, \quad \frac{1}{hl} r_\infty^{k+1} < \theta, \quad \frac{1}{hl} s_\infty^{k+1} < \theta. \quad (8)$$

Here, θ is a threshold on displacement changes applied to all three metrics. The primal residual captures the worst-case consensus mismatch on shared bodies and is defined as

$$\mathbf{r}_{i,b}^{k+1} := \mathbf{q}_{i,b}^{k+1} - \mathbf{z}_b^{k+1}, \quad r_\infty^{k+1} := \max_{b \in \mathcal{B}_\partial} \max_{i \in \mathcal{W}_b} \|\mathbf{r}_{i,b}^{k+1}\|_\infty. \quad (9)$$

The dual residual measures the change of the merged consensus state:

$$\mathbf{s}_b^{k+1} := \mathbf{z}_b^{k+1} - \mathbf{z}_b^k, \quad s_\infty^{k+1} := \max_{b \in \mathcal{B}_\partial} \|\mathbf{s}_b^{k+1}\|_\infty. \quad (10)$$

A penetration-free check is enforced to ensure feasibility of the synchronized state; see Sec. 4.2 for details. After convergence, shared bodies are merged by replacing all local replicas $\mathbf{q}_{i,b}$ with the corresponding consensus states \mathbf{z}_b .

4.2 Penetration-Free Consensus Update

In our formulation, each worker evolves its local configuration \mathbf{q}_i , while \mathbf{z} serves only as an auxiliary consensus variable in ADMM. Each local solve produces a penetration-free \mathbf{q}_i , but \mathbf{z} may be interpenetrating. As a result, even after ADMM has converged, applying

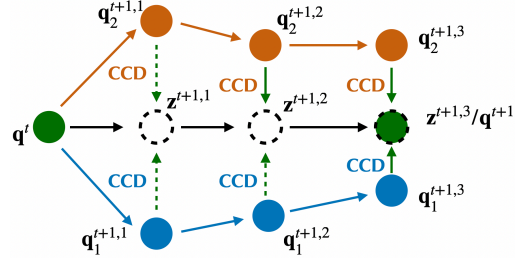


Fig. 3. Illustration of our CCD check process. We show one shared body evolving from \mathbf{q}^t to \mathbf{q}^{t+1} in a two-worker solve, where blue/orange denote the local copies on worker 1/2. Each ADMM iteration updates $\mathbf{q}_i^{t+1,k}$ by a local solve and then forms the consensus \mathbf{z}^k . To ensure a penetration-free step, we run CCD from each $\mathbf{q}_i^{t+1,k}$ toward \mathbf{z}^k . In the figure, green dashed lines indicate failed checks (TOI \neq 1), while green solid lines indicate passed checks (TOI = 1). We accept $\mathbf{q}^{t+1} = \mathbf{z}^k$ only when all workers report TOI = 1.

the consensus state to shared bodies in the final merge can still introduce interpenetration.

Based on this consideration, we augment the ADMM convergence test with an additional CCD check on the merge target, as illustrated in Fig. 3. At iteration k , the local solve yields a penetration-free \mathbf{q}_i^{k+1} , while the consensus step produces the shared-body estimate \mathbf{z}^{k+1} . A candidate merged state $\hat{\mathbf{q}}_i^{k+1}$ is constructed by replacing every shared body $b \in \mathcal{B}_{i,\partial}$ in \mathbf{q}_i^{k+1} with \mathbf{z}_b^{k+1} . CCD is then performed along the trajectory from \mathbf{q}_i^{k+1} to $\hat{\mathbf{q}}_i^{k+1}$. Convergence is accepted only if this check passes on every worker, ensuring that the consensus state can be safely applied without introducing penetration.

Discussion. With CCD enforced, a natural concern is whether repeated CCD failure could hinder convergence. We observe this issue is effectively mitigated by an adaptive time-stepping strategy. To examine this corner case, we construct the two-worker example in Fig. 4, where two replicas of the same body are driven onto opposite sides of an obstacle using a large velocity and time step. This configuration is highly artificial, requiring a horizontal force on the order of $586\times$ the body’s weight. In this case, the obstacle blocks the direct merge path. Reducing the step size allows the replicas to move around the obstacle and eventually merge. Across all other experiments, we observe no CCD-induced non-convergence.

4.3 Mass-aware Penalty Parameter Adaptation

The penalty parameter ρ plays a critical role in the convergence of ADMM. When ρ is too small, the consensus penalty is too weak to effectively reduce discrepancies among split degrees of freedom, resulting in slow agreement across partitions. Conversely, when ρ is too large, the quadratic penalty dominates the local subproblems, pulling updates aggressively toward the consensus variables and limiting progress on the original objective. We initialize the ADMM penalty parameter ρ using a mass-aware strategy, and further refine it through residual-driven adaptation during the iterations.

Mass-aware stiffness estimation. We set the initial value of ρ by $\rho_{i,b} = \beta m_b$, where β is a user-specified factor. Unless stated otherwise, we set $\beta = 1$ in all experiments. A common strategy in prior ADMM-based solvers is to scale the penalty parameter

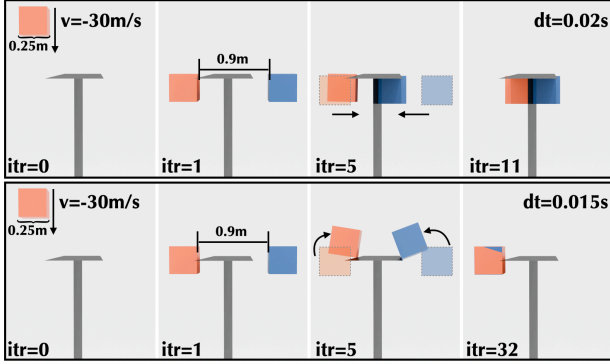


Fig. 4. A CCD-check corner case with a fixed blocking obstacle. In both rows, the duplicated body starts with the same downward velocity ($v = -30$ m/s) and the same replica separation (0.9 m) at $itr = 1$. The dashed silhouettes indicate the replica positions at $itr = 1$, and the arrows illustrate their subsequent motion directions during ADMM iterations. With $dt = 0.02$ s (top), the merge path is blocked and the replicas cannot merge. Reducing the time step to $dt = 0.015$ s (bottom) alleviates this issue and allows the replicas to gradually move around the obstacle and eventually merge.

using stiffness-related curvature proxies, such as eigenvalue-based statistics of local Hessian/constraint blocks [Brown and Narain 2021; Fang et al. 2019; Overby et al. 2017]. Following this strategy, for a body b on worker i (with DoFs $\mathbf{q}_{i,b}$), one may analyze the stiffness of the Hessian diagonal block

$$\mathbf{H}_{i,b} = \mathbf{M}_{i,b} + \mathbf{H}_{i,b}^{\text{ARAP}} + \mathbf{H}_{i,b}^{\text{IPC}}, \quad (11)$$

where $\mathbf{M}_{i,b}$, $\mathbf{H}_{i,b}^{\text{ARAP}}$, and $\mathbf{H}_{i,b}^{\text{IPC}}$ denote the contributions from inertia, elasticity, and the IPC barrier, respectively. However, directly conducting eigen analysis, e.g. using $\lambda_{\max}(\mathbf{H}_{i,b})$ or the average of $\lambda(\mathbf{H}_{i,b})$ can severely overestimate the effective stiffness, because the largest eigenvalues of $\mathbf{H}_{i,b}$ are often induced by only a few constrained modes in the ARAP and IPC terms.

Specifically, for ARAP, the largest eigenvalues mainly correspond to the three scaling modes, and can reach 10^8 in our experiments (given a Young’s modulus of 10^{12}), which easily dominates $\lambda_{\max}(\mathbf{H}_{i,b})$. Besides, the IPC term is a log-barrier function. When two bodies are very close, its associated eigenvalues can become extremely large. Moreover, this barrier only penalizes the relative-motion directions that change d , so the resulting large curvature can again dominate $\lambda_{\max}(\mathbf{H}_{i,b})$ and yield an overly conservative stiffness proxy [Daviet 2020]. In addition, barrier pairs may occasionally activate and deactivate across iterations as distances fluctuate around the activation threshold \hat{d} , making the curvature contribution of $\mathbf{H}_{i,b}^{\text{IPC}}$ highly transient. Therefore, we exclude the ARAP and IPC terms in stiffness estimation and rely only on the inertial block $\mathbf{M}_{i,b}$. In the ABD formulation, $\mathbf{M}_{i,b}$ has a simple spectral bound: its largest eigenvalue satisfies $\lambda_{\max}(\mathbf{M}_{i,b}) \leq m_b$, so we use the body mass m_b as a simple stiffness proxy. The derivation is provided in the supplementary material.

Residual-driven adaptation of ρ . In contact-rich distributed ABD simulation, although the consensus requirement itself remains unchanged, the appropriate enforcement strength varies as contacts

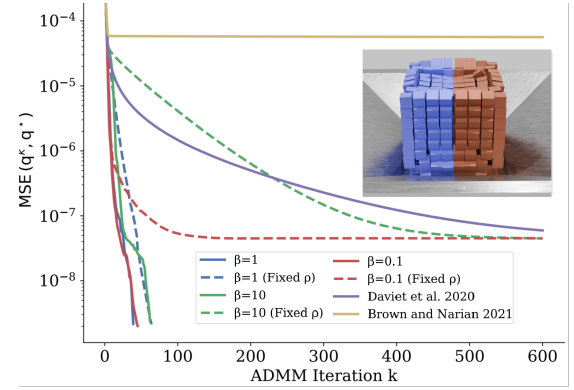


Fig. 5. Convergence comparison of ρ adaptation methods. MSE to a single-worker reference solution \mathbf{q}^* versus ADMM iterations, comparing our update to prior rules [Brown and Narain 2021; Daviet 2020].

activate, deactivate, and redistribute coupling across partitions. To account for this effect, we introduce an *adaptive consensus* mechanism that dynamically regulates the ADMM penalty parameter ρ via residual-driven, per-body adaptation, allowing the consensus strength to respond to heterogeneous convergence rate induced by varying contact states and coupling intensity. Following the residual-driven adaptation scheme of Boyd et al. [2011], we update the per-body penalty parameter ρ_b as

$$\rho_b^{k+1} = \begin{cases} \tau \rho_b^k, & \|\mathbf{r}_b^k\|_{\infty} > \mu \|\mathbf{s}_b^k\|_{\infty}, \\ \rho_b^k / \tau, & \|\mathbf{s}_b^k\|_{\infty} > \mu \|\mathbf{r}_b^k\|_{\infty}, \\ \rho_b^k, & \text{otherwise.} \end{cases} \quad (12)$$

where \mathbf{r}_b^k and \mathbf{s}_b^k denote the primal and dual residuals of body b at iteration k . By comparing these residuals, ρ_b is adjusted to balance global consistency and local objective progress. We employ multiplicative updates with threshold μ for rapid imbalance correction while avoiding sensitivity to residual noise. For numerical stability, ρ_b is clamped to a bounded range around its initial mass-aware value. Unless otherwise stated, we use $\tau = 2$, $\mu = 5$, and clamp ρ_b to $[\sigma_{\min}\rho^0, \sigma_{\max}\rho^0]$. In our experiments, we set $\sigma_{\min} = 0.001$ and $\sigma_{\max} = 1000$.

We evaluate our penalty-parameter strategy in a two-worker scene with 512 ABD bodies shown in Fig. 5, comparing against the dynamic-penalty methods of [Brown and Narain 2021; Daviet 2020]. A non-distributed ABD solution serves as the reference state \mathbf{q}^* . We then run the same scene on two nodes and report, at the k -th ADMM iteration, the mean squared error (MSE) between \mathbf{q}^k and \mathbf{q}^* . Our method rapidly reduces the error and reaches near-reference accuracy within 80 iterations. In contrast, [Brown and Narain 2021] shows little progress beyond the initial drop due to setting ρ based on a very large ARAP stiffness, while [Daviet 2020] converges faster but remains noticeably slower than our approach. We further validate the effectiveness of residual-driven adaptation: for both $\beta = 10$ and $\beta = 0.1$, enabling this update consistently converges faster than a fixed ρ and drives the solution closer to \mathbf{q}^* .

ALGORITHM 1: Consensus ADMM on worker i

Input: $N_i, \mathcal{B}_{i,\partial}, K$

```

1 fetch  $\{\mathbf{M}_b, \text{id}_b, \mathbf{q}_b, \hat{\mathbf{q}}_b\}_{b \in \mathcal{B}_{i,\partial}}$  from  $j \in N_i$  // init frame
2 build local data and  $\tilde{\mathbf{q}}_i$ 
3  $\mathbf{z}_i^1 \leftarrow \tilde{\mathbf{q}}_i, \mathbf{u}_i^1 \leftarrow \mathbf{0}$  // init ADMM
4 for  $k = 1$  to  $K$  do
5   if  $k > 1$  then
6     // fetch shared-body states
7     fetch  $\{\mathbf{q}_{j,b}^k, \rho_b^k, \mathbf{u}_{j,b}^k\}_{j \in N_i, b \in \mathcal{B}_{ij}}$ 
8     // consensus and dual updates
9     update  $\mathbf{z}_i^k$  and  $\mathbf{u}_i^k$  using Eq. (6) and Eq. (7)
10    // evaluate stopping metrics
11    evaluate  $\|\Delta \mathbf{q}_i^{k+1}\|_\infty, \mathbf{r}_i^k, \mathbf{s}_i^k$ , and  $\text{TOI}_i^k$ 
12    // controller communication
13    report  $(\|\Delta \mathbf{q}_i^{k+1}\|_\infty, \mathbf{r}_i^k, \mathbf{s}_i^k, \text{TOI}_i^k)$  to controller
14    receive signal  $\sigma$ 
15    if  $\sigma = \text{end}$  then
16      | break
17    end
18    update  $\rho_b^{k+1}$  for  $b \in \mathcal{B}_{i,\partial}$  // penalty update
19  end
20  solve Eq. (5) for  $\mathbf{q}_i^{k+1}$  // local solve
21 end
22 assign converged shared states and end the frame

```

5 Implementation Details

5.1 Distributed System Overview

Overview. Our system adopts a single-controller, multi-worker architecture, where the controller orchestrates the simulation loop and global convergence via frame-level commands. Workers are GPU-equipped nodes that perform local Newton solves and communicate only with the controller and neighboring workers under the partition model in Fig. 2. We summarize the system pipeline in Algorithm 1. At the beginning of each frame, worker i fetches the shared-body data from its neighbors, builds the local frame data, and initializes $\mathbf{z}_i^1 = \tilde{\mathbf{q}}_i$ and $\mathbf{u}_i^1 = \mathbf{0}$ (Lines 1–3). The fetched data include the mass matrices, mesh identifiers, and current states $\mathbf{q}_b, \hat{\mathbf{q}}_b$ of the shared bodies. The worker then enters the ADMM loop (Lines 4–14). For $k > 1$, it fetches the current shared-body quantities $\mathbf{q}_{j,b}^k, \rho_b^k, \mathbf{u}_{j,b}^k$, updates \mathbf{z}_i^k and \mathbf{u}_i^k , and evaluates the local stopping metrics $\|\Delta \mathbf{q}_i^{k+1}\|_\infty, \mathbf{r}_i^k, \mathbf{s}_i^k$, and TOI_i^k (Lines 6–8). These quantities are reported to the controller, which aggregates all worker reports, checks the global stopping criterion, and broadcasts the control signal (Line 9). Worker i then either terminates if $\sigma = \text{end}$ or continues otherwise (Lines 10–12). If the iteration continues, it updates ρ_b^{k+1} for the shared bodies and solves Eq. (5) for \mathbf{q}_i^{k+1} (Lines 13–14). After convergence, it assigns the converged shared states and finalizes the frame (Line 15).

5.2 Control-based Load Balancing

To mitigate load imbalance, we use a lightweight discrete-time PD controller [Strm and Hgglund 1995] that updates partition boundaries from per-frame timing feedback. Each boundary plane Γ_{ij} is parameterized by a point $\mathbf{p}_{i,j}$ and a unit normal $\mathbf{n}_{i,j}$ oriented from

worker i to worker j . In the two-worker case, let τ_i^k be the smoothed compute time of worker i at frame k , and define $\eta^k = \tau_1^k / \tau_2^k$. We normalize the imbalance as

$$T^k = \frac{\eta^k - 1}{\eta^k + 1} \in (-1, 1), \quad (13)$$

where $T^k = 0$ indicates perfect balance and the sign indicates which worker is slower. We compute a PD update

$$\Delta \mathbf{p}_{1,2}^k = K_P T^k + K_D (T^k - T^{k-1}), \quad (14)$$

and shift the boundary along its normal, $\mathbf{p}_{1,2} := \mathbf{p}_{1,2} + \Delta \mathbf{p}_{1,2}^k \mathbf{n}_{1,2}$, to redistribute workload between the two workers.

6 Experiments

We implemented the distributed simulation system on a multi-node cluster based on a cloud environment. Each node is equipped with an AMD EPYC 7402 CPU (10 cores, 2.79 GHz), 32 GB of system memory and a single NVIDIA RTX 4090 GPU. Nodes are connected via Ethernet with a peak bandwidth of 1 Gb/s. In this section, we report scaling tests, results on the mass-aware penalty adaptation strategy, and large-scale simulations. Additional results on dynamic load balancing, parameter sensitivity, and partition orientation, as well as detailed experimental settings, are provided in the supplementary material.

6.1 Multi-worker Scaling

We evaluate multi-worker scalability by measuring speedup with increasing workers. We simulate a fixed large-scale scene consisting of 29,760 spheres falling into a square container under gravity. The number of workers is varied by partitioning the same domain into $N \in \{1, 2, 4, 8\}$. As shown in Fig. 6, near-linear speedup is achieved with 2 and 4 workers. When scaling to 8 workers, the speedup decreases to about 6 \times , primarily due to stronger cross-partition coupling under finer partitioning, which leads to more ADMM iterations and a higher proportion of synchronization and interface-handling overhead. For completeness, we further conduct a weak scaling test following [Qiu et al. 2023; Wang et al. 2020] and report the results in the supplementary material.

6.2 Mass-aware Penalty Parameter Adaptation

Validation under varying mass scales. This experiment tests the effectiveness of the mass-aware initialization across different mass scales. We use a scene consisting of 512 rigid bodies falling and piling into a funnel-shaped container, distributed across two workers. Fig. 11 shows that the mass-aware initialization is robust across all tested mass scales.

To study robustness across mass scales, we vary body density while keeping the geometry fixed, using five density levels: 10, 100, 1,000, 10,000, and 100,000 kg/m³. For each density level, the initial penalty for body b is set as $\rho_b^0 = \beta m_b$, where m_b denotes the body mass and $\beta \in \{0.01, 0.1, 1.0, 10, 100\}$. In particular, $\beta = 1.0$ gives the lowest or near-lowest iteration count across all density levels, while $\beta = 0.1$ also performs well. This suggests that the mass-aware initialization is robust across a wide range of mass scales. The main outlier is the lightest case, 10 kg/m³, with $\beta = 10^{-2}$. In this

Table 1. Large-scale experiment statistics. Number of ADMM iterations and timings are averaged over the entire simulation, while collision candidate and contact counts are reported as peak values. Timing results are reported per frame, where t_{solve} measures the time spent in local Newton solve, t_{coll} accounts for collision detection, t_{sync} denotes synchronization and communication overhead, and t_{frame} is the total elapsed frame time. For the rigid-fluid coupling example, the object count reported as 1M + 8 refers to one million fluid particles interacting with eight rigid bodies.

Example	# Worker	# DoF	# Objects	# Triangle	# Candidate	# Contact	$h(s)$	# ADMM Iter	$t_{\text{solve}}(s)$	$t_{\text{coll}}(s)$	$t_{\text{sync}}(s)$	$t_{\text{frame}}(s)$
“Pokémon”	2	62.4K	5.2K	5.7M	59.8M	40.1K	0.0125	75.85	18.40	21.90	3.41	44.06(1.7×)
Food Falling	6	313.5K	26.1K	16.1M	164.7M	222.6K	0.01	77.57	22.29	28.88	7.03	58.64(5.2×)
Drum and Shells	2	27.9K	2.3K	4.0M	53.6M	20.0K	0.006	51.46	6.20	17.34	2.44	26.34(1.5×)
Parts and Robotic Arm	4	85.5K	7.1K	13.0M	452.9M	338.4K	0.01	91.52	19.69	67.77	4.66	92.76(∞)
Rigid-Fluid Coupling	4	3.1M	1.0M + 8	219.6K	3.3M	133.6K	0.003	10.28	0.40	0.63	0.06	1.09

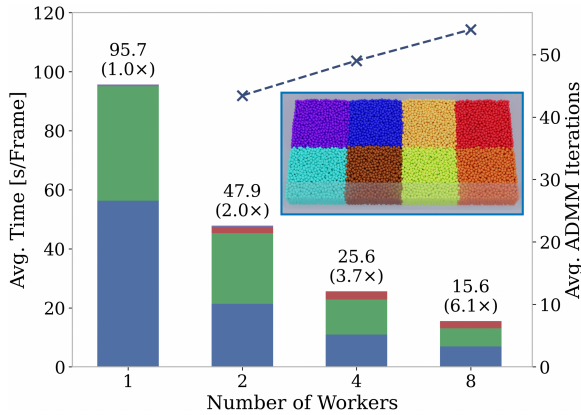


Fig. 6. Scaling results on the same scene partitioned into $\{1, 2, 4, 8\}$ workers. The inset shows the final state of the simulation with 8 workers. The stacked bars report the breakdown of the average time per frame, including Newton solve time (blue), collision detection time (green), synchronization time (red), and other overheads (purple). The dashed line shows the average number of ADMM iterations.

case, ρ_b^0 becomes too small, so the consensus penalty is too weak to effectively enforce agreement among workers, which leads to slower ADMM convergence.

Ablation of residual-driven ρ adaptation. We evaluate residual-driven adaptation of the ADMM penalty parameter in the same two-worker scene with 512 rigid bodies. The mass-based initialization is fixed to $\beta = 1.0$ (i.e., $\rho_b^0 = m_b$), and we compare convergence with and without residual-driven adaptation. For each density level, the average number of ADMM iterations required to reach the same stopping criteria is measured. As shown in Fig. 12, enabling residual-driven adaptation reduces the iteration count by 22%–80% across all density levels compared to using a fixed penalty parameter.

Validation under material heterogeneity. Our method remains robust under large mass and stiffness contrasts. We construct a two-worker scene with 200 bodies, divided into three groups with $(m, E) = (1, 10^8)$, $(100, 10^{10})$, and $(10^4, 10^{12})$. The scene is visualized in Fig. 13. We compare this setting with a homogeneous baseline where all bodies use $(100, 10^{10})$. In the homogeneous case, the distributed solver requires about 2× more ADMM iterations and 2.5× more Newton iterations as reported in Table 2. This increase mainly reflects the greater difficulty of the underlying ABD problem, rather than the distributed ADMM scheme itself. To verify this, we

Table 2. Effect of mass and stiffness heterogeneity on convergence. Here, 2W and 1W denote two-worker and single-worker settings, respectively; “hetero.” denotes the heterogeneous setting, and “uniform” denotes the uniform setting.

Case	# ADMM Iter	# Newton Iter
2W, hetero.	66.82	147.49
2W, uniform	36.11	60.13
1W, hetero.	–	94.72
1W, uniform	–	37.15

also run the same setting on a single worker, where the Newton iteration count likewise increases by about 2.5×. We further vary the mass-aware coefficient β to evaluate the proposed initialization. Detailed results are provided in the supplementary material.

6.3 Large-scale Distributed Simulation

Large-scale ABD simulation scenarios are used to demonstrate the capability and robustness of the proposed system, including numerical stability, high collision resolution, and effective scaling in distributed environments. Table 1 summarizes detailed statistics and configuration parameters for all experiments. To clarify the reported collision statistics, we refer to broad-phase outputs as candidate collision pairs and to pairs retained after narrow-phase filtering as active contact pairs [Ericson 2004].

“Pokémon”. We simulate a “Pokémon” scenario in which objects fall through a narrow funnel and interact with two perforated trays inside a container, as illustrated in Fig. 1. The simulation involves 5,203 rigid bodies with 5.7M triangles, distributed across two workers. Bodies are released from above, pass through the funnel, and land on two stacked rotating perforated plates. Some bodies remain on the plates, while others fall through the holes and reach the container bottom. During the simulation, we handle up to 59.8M candidate collision pairs and 40.1K active contact pairs. Interpenetration does not occur at any point during the simulation. Average wall-clock time is 44.06s per frame for this example, a 1.7× improvement over single-worker execution.

Falling foods. We simulate a large-scale dropping scenario consisting of 27,163 ABD bodies distributed across six workers, leading to extreme geometric complexity and collision density as the container fills. Fig. 7 shows the resulting dynamics. The simulation involves 16M triangles and reaches up to 164M collision candidates with 222K active contact pairs. Despite the heavy collision workload,

penetration-free configurations are maintained throughout the simulation. In this simulation, the average frame time is 58.64 s, achieving a 5.2× speedup over a single-worker baseline.

Industrial parts and robotic arm. We also test an industrial part lifting task driven by a robotic arm, simulated on four workers with 7,124 ABD bodies. A container with a pull ring is placed at the scene center, and the robotic arm successfully grasps the ring and lifts the container. The simulation includes over 13M triangles and produces 452M collision candidates and 338K active contact pairs during the dropping and lifting stages. Fig. 8 contains rendered snapshots from this experiment. On average, this case takes 92.76s per frame on four workers, whereas a single-GPU setup cannot accommodate the case due to insufficient GPU memory. The simulation remains penetration-free across all frames.

Rotating drum with shells. We simulate a rotating-drum scenario on two workers with 2,323 rigid bodies and 4M triangles. As in Fig. 9, the drum acts as a moving boundary and continuously agitates bodies with sharp, non-convex shapes, causing repeated mixing and piling inside the drum. The complex body geometries sustain a heavy collision workload and generate up to 54M collision candidates. Collision detection dominates the computation and accounts for 66% of the total runtime, as reported in Table 1. With two workers, the simulation remains penetration-free and runs at 26.34s per frame on average, and the resulting speedup over a single worker is 1.5 ×.

Rigid-fluid coupling. We further evaluate the scalability of our distributed ABD framework by applying it to fluid simulation and rigid-fluid coupling. We implement an IISPH [Ihmsen et al. 2013] solver and integrate it into our distributed system according to [Rustico et al. 2012]. As for the rigid-fluid coupling, we implement a simple impulse-based method [Becker et al. 2009] to compute the two-way coupling force at the beginning of each frame and apply the resulting coupling force to both fluid particles and rigid bodies as external forces. In this case, we use $h = 0.003$ and $\theta = 0.0008$ and assign 4 workers with 1M fluid particles and 220K triangles for ABD objects. The results are visualized in Fig. 10. The average run time of this experiment is 1.09s per frame.

7 Conclusion

In this work, we present a distributed ABD framework based on ADMM that enables penetration-free simulation across multiple GPU workers, allowing large-scale contact handling in a distributed environment. To address the sensitivity of ADMM to the penalty parameter, we initialize ρ based on object mass and further refine it through residual-driven adaptation, significantly accelerating convergence. With a lightweight load-balancing scheme, experiments on large-scale, contact-rich scenarios demonstrate stable, penetration-free simulation and near-linear speedups in multi-node distributed settings.

Limitations and future work. Our current implementation relies on blocking communication and does not overlap data transfer with local computation, causing communication latency to directly

contribute to the overall runtime. Incorporating asynchronous communication together with latency-hiding mechanisms could substantially reduce the effective communication overhead and further improve scalability. Moreover, our experiments indicate that finer partitioning leads to an increased number of ADMM iterations, potentially offsetting the benefits of improved load balance. Exploring more effective warm-start strategies or partition-aware initialization will be a valuable direction. Finally, ADMM may converge slowly when high accuracy is required, often exhibiting a long tail near convergence. To this end, we plan to explore Anderson acceleration and related techniques to mitigate this long-tail slowdown and reduce the total number of iterations.

Acknowledgments

We would like to sincerely thank all the reviewers for their valuable and constructive comments and suggestions. Weiwei Xu is partially supported by NSFC (92570206, 62421003), and State Key Laboratory of CAD&CG, Zhejiang University. Yin Yang is partially supported by NSF 2301040. Yifan Peng is partially supported by the National Natural Science Foundation of China (62322217) and the Innovation and Technology Fund of Hong Kong (MHP/313/24).

References

- Jose A Barreiros, Aykut Özgün Önel, Mengchao Zhang, Sam Creasey, Aimee Goncalves, Andrew Beaulieu, Aditya Bhat, Kate M Tsui, and Alex Alspach. 2025. Learning contact-rich whole-body manipulation with example-guided reinforcement learning. *Science Robotics* 10, 105 (2025), eads6790.
- Markus Becker, Hendrik Tessenendorf, and Matthias Teschner. 2009. Direct forcing for lagrangian rigid-fluid coupling. *IEEE Transactions on Visualization and Computer Graphics* 15, 3 (2009), 493–503.
- Stephen Boyd, Neal Parikh, Eric Chu, Borja Peleato, Jonathan Eckstein, et al. 2011. Distributed optimization and statistical learning via the alternating direction method of multipliers. *Foundations and Trends® in Machine Learning* 3, 1 (2011), 1–122.
- Alexander James Ronald Brown. 2020. *Distributed real-time physics for scalable and streamed games and simulation*. Ph. D. Dissertation. Newcastle University.
- George E Brown and Rahul Narain. 2021. Wrapd: weighted rotation-aware admm for parameterization and deformation. *ACM Transactions on Graphics (TOG)* 40, 4 (2021), 1–14.
- Tony F Chan and Tarek P Mathew. 1994. Domain decomposition algorithms. *Acta numerica* 3 (1994), 61–143.
- Anka He Chen, Jerry Hsu, Ziheng Liu, Miles Macklin, Yin Yang, and Cem Yuksel. 2025. Offset Geometric Contact. *ACM Transactions on Graphics (TOG)* 44, 4 (2025), 1–21.
- Yunuo Chen, Minchen Li, Lei Lan, Hao Su, Yin Yang, and Chenfanfu Jiang. 2022. A unified newton barrier method for multibody dynamics. *ACM Transactions on Graphics (TOG)* 41, 4 (2022), 1–14.
- Yi-Lu Chen, Mickaël Ly, and Chris Wojtan. 2023. Unified treatment of contact, friction and shock-propagation in rigid body animation (*SCA '23*). Association for Computing Machinery, New York, NY, USA, Article 5, 2 pages. doi:10.1145/3606037.3606836
- Gilles Daviet. 2020. Simple and scalable frictional contacts for thin nodal objects. *ACM Transactions on Graphics (TOG)* 39, 4 (2020), 61–1.
- Gilles Daviet. 2023. Interactive hair simulation on the GPU using ADMM. In *ACM SIGGRAPH 2023 Conference Proceedings*. 1–11.
- Jeffrey Dean and Sanjay Ghemawat. 2008. MapReduce: simplified data processing on large clusters. *Commun. ACM* 51, 1 (2008), 107–113.
- Christer Ericson. 2004. *Real-time collision detection*. Crc Press.
- Yu Fang, Minchen Li, Ming Gao, and Chenfanfu Jiang. 2019. Silly rubber: an implicit material point method for simulating non-equilibrated viscoelastic and elastoplastic solids. *ACM Transactions on Graphics (TOG)* 38, 4 (2019), 1–13.
- Zachary Ferguson, Minchen Li, Teseo Schneider, Francisca Gil-Ureta, Timothy Langlois, Chenfanfu Jiang, Denis Zorin, Danny M Kaufman, and Daniele Panozzo. 2021. Intersection-free rigid body dynamics. *ACM Transactions on Graphics* 40, 4 (2021).
- Yuan Yu Michael Isard Dennis Fetterly, Mihai Budiu, Úlfar Erlingsson, and Pradeep Kumar Gunda Jon Currey. 2009. DryadLINQ: A system for general-purpose distributed data-parallel computing using a high-level language. *Proc. LIDS-IR* 8 (2009), 1–14.
- William D. Gropp. 2001. Learning from the Success of MPI. In *High Performance Computing — HiPC 2001 (Lecture Notes in Computer Science, Vol. 2228)*, Burkhard

- Monien, Viktor K. Prasanna, and Sriram Vajapeyam (Eds.). Springer, 81–94. doi:10.1007/3-540-45307-5_8
- Dewen Guo, Minchen Li, Yin Yang, Sheng Li, and Guoping Wang. 2024. Barrier-Augmented Lagrangian for GPU-based Elastodynamic Contact. *ACM Transactions on Graphics (TOG)* 43, 6 (2024), 1–17.
- Kemeng Huang, Floyd M Chitalu, Huancheng Lin, and Taku Komura. 2024a. GIPC: Fast and stable gauss-newton optimization of IPC barrier energy. *ACM Transactions on Graphics* 43, 2 (2024), 1–18.
- Kemeng Huang, Xinyu Lu, Huancheng Lin, Taku Komura, and Minchen Li. 2024b. StiffGIPC: Advancing GPU IPC for stiff affine-deformable simulation. *arXiv preprint arXiv:2411.06224* (2024).
- Markus Ihmsen, Jens Cornelis, Barbara Solenthaler, Christopher Horvath, and Matthias Teschner. 2013. Implicit incompressible SPH. *IEEE transactions on visualization and computer graphics* 20, 3 (2013), 426–435.
- Tiffany Inglis, M-L Eckert, James Gregson, and Nils Thuerey. 2017. Primal-dual optimization for fluids. In *Computer Graphics Forum*, Vol. 36. Wiley Online Library, 354–368.
- Harim Ji, Hyunsu Kim, Jeongmin Lee, Somang Lee, Seoki An, Jinuk Heo, Youngseon Lee, Yongseok Lee, and Dongjun Lee. 2025. GPU-Accelerated Subsystem-Based ADMM for Large-Scale Interactive Simulation. In *JCRA 2025 Workshop "Handy Moves: Dexterity in Multi-Fingered Hands" Paper Submission*.
- Manas Anand Kale. 2023. *Distributed Simulation of Large Multi-body Systems*. McGill University (Canada).
- Lei Lan, Danny M. Kaufman, Minchen Li, Chenfanfu Jiang, and Yin Yang. 2022a. Affine body dynamics: fast, stable and intersection-free simulation of stiff materials. 41, 4, Article 67 (July 2022), 14 pages. doi:10.1145/3528223.3530064
- Lei Lan, Minchen Li, Chenfanfu Jiang, Huamin Wang, and Yin Yang. 2023. Second-order Stencil Descent for Interior-point Hyperelasticity. *ACM Trans. Graph.* 42, 4, Article 108 (July 2023), 16 pages. doi:10.1145/3592104
- Lei Lan, Zixuan Lu, Jingyi Long, Chun Yuan, Xuan Li, Xiaowei He, Huamin Wang, Chenfanfu Jiang, and Yin Yang. 2024. Efficient GPU cloth simulation with non-distance barriers and subspace reuse. *arXiv preprint arXiv:2403.19272* (2024).
- Lei Lan, Guanqun Ma, Yin Yang, Changxi Zheng, Minchen Li, and Chenfanfu Jiang. 2022b. Penetration-free projective dynamics on the GPU. *ACM Transactions on Graphics (TOG)* 41, 4 (2022), 1–16.
- Jeongmin Lee, Minji Lee, and Dongjun Lee. 2023. Modular and parallelizable multibody physics simulation via subsystem-based ADMM. *arXiv preprint arXiv:2302.14344* (2023).
- Steve Lesser, Alexey Stomakhin, Gilles Daviet, Joel Wretborn, John Edholm, Noh-Hoon Lee, Eston Schweickart, Xiao Zhai, Sean Flynn, and Andrew Moffat. 2022. Loki: a unified multiphysics simulation framework for production. *ACM Transactions on Graphics (TOG)* 41, 4 (2022), 1–20.
- Cheng Li, Min Tang, Ruofeng Tong, Ming Cai, Jieyi Zhao, and Dinesh Manocha. 2020c. P-Cloth: Interactive Cloth Simulation on Multi-GPU Systems using Dynamic Matrix Assembly and Pipelined Implicit Integrators. *ACM Transaction on Graphics (Proceedings of SIGGRAPH Asia)* 39, 6 (December 2020), 180:1–15.
- Minchen Li, Zachary Ferguson, Teseo Schneider, Timothy Langlois, Denis Zorin, Daniele Panozzo, Chenfanfu Jiang, and Danny M. Kaufman. 2020a. Incremental Potential Contact: Intersection- and Inversion-free Large Deformation Dynamics. *ACM Trans. Graph. (SIGGRAPH)* 39, 4, Article 49 (2020).
- Minchen Li, Danny M Kaufman, and Chenfanfu Jiang. 2020b. Codimensional incremental potential contact. *arXiv preprint arXiv:2012.04457* (2020).
- Xuan Li, Yu Fang, Lei Lan, Huamin Wang, Yin Yang, Minchen Li, and Chenfanfu Jiang. 2023. Subspace-preconditioned gpu projective dynamics with contact for cloth simulation. In *SIGGRAPH Asia 2023 Conference Papers*. 1–12.
- Haixiang Liu, Nathan Mitchell, Mridul Aanjaneya, and Eftychios Sifakis. 2016. A scalable schur-complement fluids solver for heterogeneous compute platforms. *ACM Transactions on Graphics (TOG)* 35, 6 (2016), 1–12.
- Xiaoxiao Long, Qingrui Zhao, Kaiwen Zhang, Zihao Zhang, Dingrui Wang, Yumeng Liu, Zhengjie Shu, Yi Lu, Shouzheng Wang, Xinzhe Wei, Wei Li, Wei Yin, Yao Yao, Jia Pan, Qiu Shen, Ruigang Yang, Xun Cao, and Qionghai Dai. 2025. A Survey: Learning Embodied Intelligence from Physical Simulators and World Models. (07 2025). doi:10.48550/arXiv.2507.00917
- Yucheng Low, Joseph Gonzalez, Aapo Kyröla, Danny Bickson, Carlos Guestrin, and Joseph M Hellerstein. 2012. Distributed graphlab: A framework for machine learning in the cloud. *arXiv preprint arXiv:1204.6078* (2012).
- Omid Mashayekhi, Chinmayee Shah, Hang Qu, Andrew Lim, and Philip Levis. 2018. Automatically distributing eulerian and hybrid fluid simulations in the cloud. *ACM Transactions on Graphics (TOG)* 37, 2 (2018), 1–14.
- Angelia Nedic and Asuman Ozdaglar. 2009. Distributed subgradient methods for multi-agent optimization. *IEEE Transactions on automatic control* 54, 1 (2009), 48–61.
- Wenqing Ouyang, Yue Peng, Yuxin Yao, Juyong Zhang, and Bailin Deng. 2020. Anderson acceleration for nonconvex ADMM based on Douglas-Rachford splitting. In *Computer Graphics Forum*, Vol. 39. Wiley Online Library, 221–239.
- Matthew Overby, George E. Brown, Jie Li, and Rahul Narain. 2017. ADMM \supseteq Projective Dynamics: Fast Simulation of Hyperelastic Models with Dynamic Constraints. *IEEE Transactions on Visualization and Computer Graphics* 23, 10 (2017), 2222–2234. doi:10.1109/TVCG.2017.2730875
- Daniel Pérez Palomar and Mung Chiang. 2006. A tutorial on decomposition methods for network utility maximization. *IEEE Journal on Selected Areas in Communications* 24, 8 (2006), 1439–1451.
- Zherong Pan and Dinesh Manocha. 2017. Efficient solver for spacetime control of smoke. *ACM Transactions on Graphics (ToG)* 36, 4 (2017), 1.
- Yue Peng, Bailin Deng, Juyong Zhang, Fanyu Geng, Wenjie Qin, and Ligang Liu. 2018. Anderson Acceleration for Geometry Optimization and Physics Simulation. *ACM Transactions on Graphics* 37, 4CD (2018), 42.1–42.14.
- Yuxing Qiu, Samuel Temple Reeve, Minchen Li, Yin Yang, Stuart Ryan Slattery, and Chenfanfu Jiang. 2023. A sparse distributed gigascale resolution material point method. *ACM Transactions on Graphics* 42, 2 (2023), 1–21.
- Eugenio Rustico, Giuseppe Bilotta, Alexis Hérault, Ciro Del Negro, and Giovanni Gallo. 2012. Advances in multi-GPU smoothed particle hydrodynamics simulations. *IEEE Transactions on Parallel and Distributed Systems* 25, 1 (2012), 43–52.
- Wei Shi, Qing Ling, Gang Wu, and Wotao Yin. 2015. Extra: An exact first-order algorithm for decentralized consensus optimization. *SIAM Journal on Optimization* 25, 2 (2015), 944–966.
- Karl Johan Strm and Tore Hggglund. 1995. PID controllers: Theory, Design and Tuning. *instrument society of america research triangle park nc* (1995).
- Alessandro Tasora, Dario Mangoni, Simone Benatti, and Rinaldo Garziera. 2021. Solving variational inequalities and cone complementarity problems in nonsmooth dynamics using the alternating direction method of multipliers. *Internat. J. Numer. Methods Engrg.* 122, 16 (2021), 4093–4113.
- Richard Tonge, Feodor Benevolenski, and Andrey Voroshilov. 2012. Mass splitting for jitter-free parallel rigid body simulation. *ACM Transactions on Graphics (TOG)* 31, 4 (2012), 1–8.
- Tianyu Wang, Jiong Chen, Dongping Li, Xiaowei Liu, Huamin Wang, and Kun Zhou. 2023. Fast GPU-based two-way continuous collision handling. *ACM Transactions on Graphics* 42, 5 (2023), 1–15.
- Xinlei Wang, Yuxing Qiu, Stuart R Slattery, Yu Fang, Minchen Li, Song-Chun Zhu, Yixin Zhu, Min Tang, Dinesh Manocha, and Chenfanfu Jiang. 2020. A massively parallel and scalable multi-GPU material point method. *ACM Transactions on Graphics (TOG)* 39, 4 (2020), 30–1.
- Tianyi Xie, Minchen Li, Yin Yang, and Chenfanfu Jiang. 2023. A contact proxy splitting method for Lagrangian solid-fluid coupling. *ACM Transactions on Graphics (TOG)* 42, 4 (2023), 1–14.
- Yu Yang, Xiaohong Guan, Qing-Shan Jia, Liang Yu, Bolun Xu, and Costas J Spanos. 2022. A survey of ADMM variants for distributed optimization: Problems, algorithms and features. *arXiv preprint arXiv:2208.03700* (2022).
- Kun Yuan, Bicheng Ying, Xiaochuan Zhao, and Ali H Sayed. 2018. Exact diffusion for distributed optimization and learning—Part I: Algorithm development. *IEEE Transactions on Signal Processing* 67, 3 (2018), 708–723.
- Matei Zaharia, Mosharaf Chowdhury, Tathagata Das, Ankur Dave, Justin Ma, Murphy McCauly, Michael J Franklin, Scott Shenker, and Ion Stoica. 2012. Resilient distributed datasets: A {Fault-Tolerant} abstraction for {In-Memory} cluster computing. In *9th USENIX symposium on networked systems design and implementation (NSDI 12)*. 15–28.
- Juyong Zhang, Yue Peng, Wenqing Ouyang, and Bailin Deng. 2019. Accelerating ADMM for efficient simulation and optimization. *ACM Transactions on Graphics (TOG)* 38, 6 (2019), 1–21.
- Juntian Zheng, Zhaofeng Luo, and Minchen Li. 2025. Robust and Efficient Penetration-Free Elastodynamics without Barriers. *arXiv preprint arXiv:2512.12151* (2025).

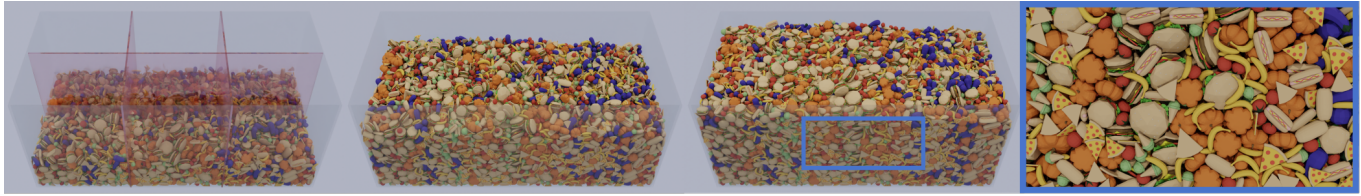


Fig. 7. *Falling foods*. A falling and piling scene with food-shaped rigid bodies, containing over 16M triangles and reaching a peak of 164M collision candidates and 222K active contact pairs. Using six workers, the distributed solver achieves a 5.2× speedup over a single-worker run. Even under such dense contact interactions, our system remains globally penetration-free and continues to exhibit near-linear scaling across workers. Note that the red planes shown in the leftmost sub-figure indicate the spatial partitioning. The same convention is used in Figs. 8 and 9.

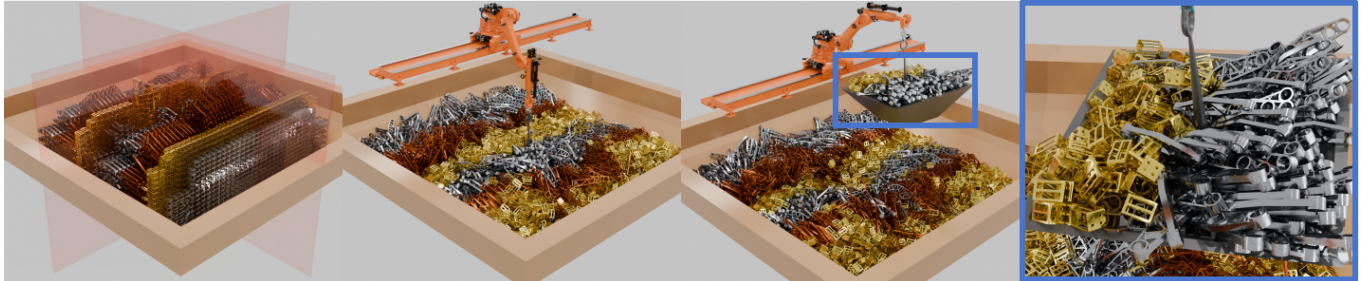


Fig. 8. *Industrial parts and robotic arm*. A large-scale scenario with 7K industrial parts and a robotic arm, totaling over 13M triangles and hundreds of millions of contact candidates. The scene cannot be executed on a single machine due to memory constraints. By distributing geometry and contact processing across workers, our system significantly reduces per-worker memory footprint, enabling simulation at scales that exceed the capacity of a single machine.

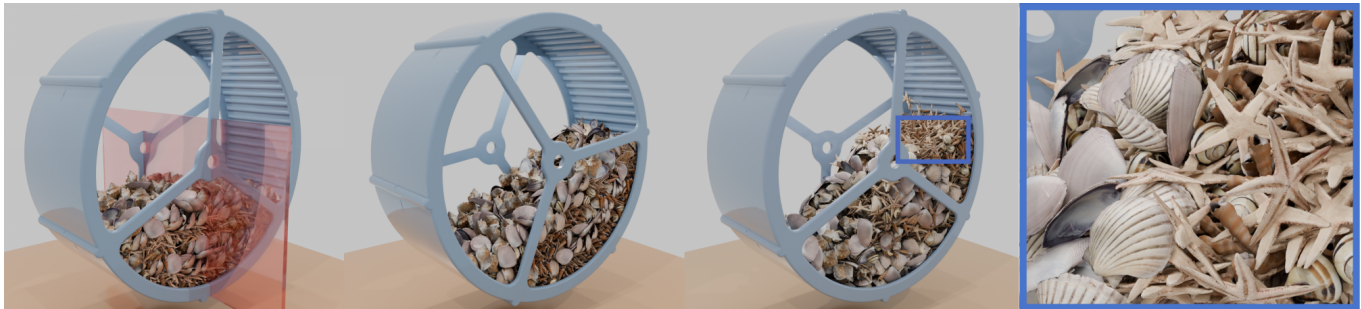


Fig. 9. *Rotating drum with shells*. Dense-contact simulation of 2K complex-shaped rigid bodies (e.g., starfish, conches, and shells) continuously agitated in a rotating drum, generating up to 54M collision candidates. The two-worker distributed solver achieves a 1.5× speedup over a single-machine run. Even in this challenging setting with thin shells and sharp features undergoing sustained agitation, our solver maintains penetration-free contact throughout the simulation.

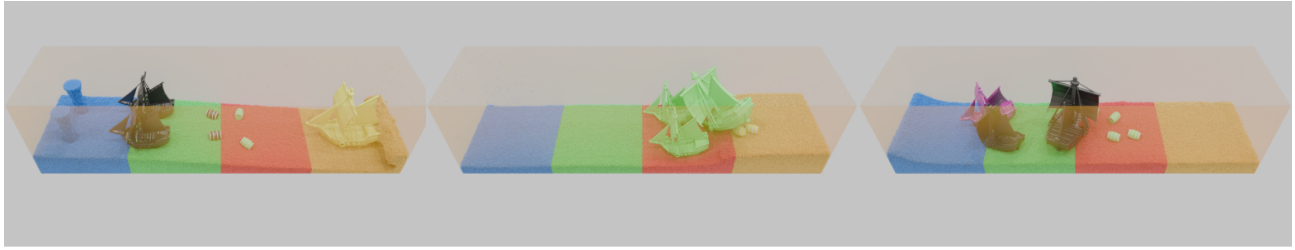


Fig. 10. *Solid-fluid coupling*. Alongside distributed ABD, our system also supports distributed fluid simulation and fluid–solid coupling. In this demo, four workers run distributed IISPH with 1M fluid particles and an ABD solid scene of 7 bodies totaling 220K triangles, with impulse-based two-way solid–fluid coupling. These results show that our multi-node architecture can support coupled multiphysics within a unified distributed framework, paving the way towards large-scale multiphysics simulation on multi-node systems.

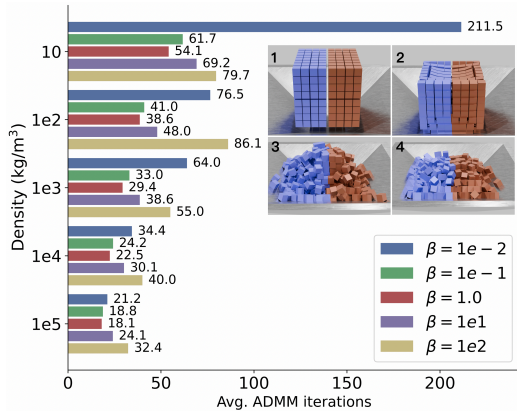


Fig. 11. Mass scaling for penalty initialization. We vary density to scale body masses and report average ADMM iterations. Initializing ρ with body mass reduces iteration counts across all settings, implying faster convergence.

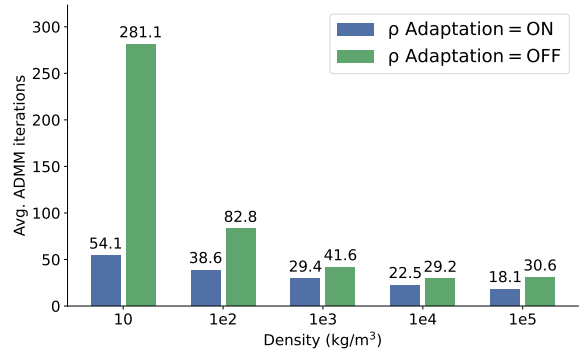


Fig. 12. Ablation of residual-driven ρ adaptation. For five mass settings, we report the average ADMM iterations with and without dynamic ρ updates.

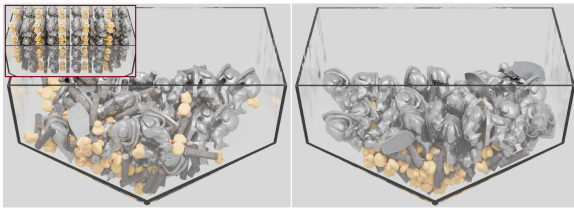


Fig. 13. Experimental scene for evaluating the effect of mass and stiffness heterogeneity. The inset at the upper left shows the initial configuration. Ducks, wooden logs, and metallic cats correspond to $(m, E) = (1, 10^8)$, $(100, 10^{10})$, and $(10^4, 10^{12})$, respectively. The left panel shows the final state of the heterogeneous setting, while the right panel shows the corresponding uniform setting with $(m, E) = (100, 10^{10})$ for all objects. Both panels share the same geometry and initial layout.